



ALMA’s Polarized View of 10 Protostars in the Perseus Molecular Cloud

Erin G. Cox¹ , Robert J. Harris^{2,1}, Leslie W. Looney¹ , Zhi-Yun Li³, Haifeng Yang³, John J. Tobin^{4,5} , and Ian Stephens⁶

¹Department of Astronomy, University of Illinois at Urbana-Champaign, 1002 W. Green Street, Urbana, IL 61801, USA; egcox2@illinois.edu

²National Center for Supercomputing Applications, University of Illinois at Urbana-Champaign, 1205 W Clark Street, Urbana, IL 61801, USA

³Department of Astronomy, University of Virginia, 530 McCormick Road, Charlottesville, VA 22903, USA

⁴Homer L. Dodge Department of Physics and Astronomy, University of Oklahoma, 440 W. Brooks Street, Norman, OK 73019, USA

⁵Leiden Observatory, Leiden University, P.O. Box 9513, 2000-RA Leiden, The Netherlands

⁶Harvard-Smithsonian Center for Astrophysics, 60 Garden Street, Cambridge, MA 02138, USA

Received 2017 November 2; revised 2018 January 29; accepted 2018 January 31; published 2018 March 12

Abstract

We present 870 μm ALMA dust polarization observations of 10 young Class 0/I protostars in the Perseus Molecular Cloud. At $\sim 0''.35$ (80 au) resolution, all of our sources show some degree of polarization, with most (9/10) showing significantly extended emission in the polarized continuum. Each source has incredibly intricate polarization signatures. In particular, all three disk-candidates have polarization vectors roughly along the minor axis, which is indicative of polarization produced by dust scattering. On ~ 100 au scales, the polarization is at a relatively low level ($\lesssim 1\%$) and is quite ordered. In sources with significant envelope emission, the envelope is typically polarized at a much higher ($\gtrsim 5\%$) level and has a far more disordered morphology. We compute the cumulative probability distributions for both the small (disk-scale) and large (envelope-scale) polarization percentage. We find that the two are intrinsically different, even after accounting for the different detection thresholds in the high/low surface brightness regions. We perform Kolmogorov–Smirnov and Anderson–Darling tests on the distributions of angle offsets of the polarization from the outflow axis. We find disk-candidate sources are different from the non-disk-candidate sources. We conclude that the polarization on the 100 au scale is consistent with the signature of dust scattering for disk-candidates and that the polarization on the envelope-scale in all sources may come from another mechanism, most likely magnetically aligned grains.

Key words: ISM: magnetic fields – polarization – stars: formation – stars: protostars

1. Introduction

High-resolution, sub/millimeter dust continuum observations of protostars preferentially probe grains that are ~ 0.1 mm to a few millimeters—the pebble-sized rocks that are the first step toward planetary bodies. These grains are responsible for continuum polarization in protostars. A few mechanisms could be responsible; each reveals a different facet of the protostar’s nascent environment. These mechanisms can depend on the grain population, opacity, and, through these, the size-scale observed (e.g., envelope/disk; Lazarian 2007; Kataoka et al. 2015, 2016a; Tazaki et al. 2017). Previous polarization surveys of protostars (Chapman et al. 2013; Hull et al. 2014; Zhang et al. 2014) have been at relatively low resolution and only probed these objects’ nascent envelope. High-resolution observations of the environment close to the protostar (\sim few hundred au, such as those done by Hull et al. 2017, in Serpens) are necessary to disentangle the emission from the envelope and disk, and therefore understand how grains change in the envelope–disk transition.

Traditionally, dust continuum polarization observations are used as a proxy for the magnetic field. Dust grains align themselves perpendicularly to the local magnetic field and consequently emit polarized thermal emission (Lazarian 2007). Observationally constraining the field’s morphology and strength is important in star formation on all scales. In the ~ 0.1 pc core where protostars will form, magnetic fields, if strong enough, control the initial collapse through both magnetic pressure support and ambipolar diffusion (e.g., Shu et al. 1987), directly influencing the timescale on which stars can form. Once the cloud has begun its collapse, infalling material can travel along these field lines from large (cloud)

scales to the small (disk) scales (Li et al. 2014). On small scales, magnetic fields are thought to play an important role in the outflows, jets, wind launching, and disk accretion (e.g., Blandford & Payne 1982; Balbus & Hawley 1998). In fact, in the youngest protostars (Class 0 sources; Andre et al. 1993), these fields may create efficient magnetic braking, hindering large ($R \sim 100$ au) disk growth until later evolutionary phases, such as the Class I phase.

Indeed, ideal MHD simulations have shown that magnetic braking can be strong in Class 0 sources (e.g., Hennebelle & Fromang 2008; Mellon & Li 2008). These simulations show that when magnetic fields are aligned with the infalling envelope’s rotation axis, the magnetic braking is efficient enough to strip infalling material of angular momentum (Hennebelle & Fromang 2008; Mellon & Li 2008). The angular momentum loss can hinder large disk formation in these sources (Li et al. 2011) until they are older Class I/II objects (e.g., Andrews et al. 2009, 2010; Mellon & Li 2009; Dapp & Basu 2010). Conversely, if the field is perpendicular or misaligned, magnetic braking is not as efficient, and a large disk may grow (e.g., Joos et al. 2012). Observations of the inferred magnetic field of Class 0 sources have shown this dependence of disk formation on field alignment to hold down to ~ 1000 to a few hundred au (e.g., Hull et al. 2014; Segura-Cox et al. 2015). Early analytic estimates of the spin-down time for rotating starless cores embedded in a non-rotating, more tenuous medium might seem to contradict this result because they indicate more efficient magnetic braking in an aligned rotator instead of an orthogonal rotator (e.g., Mouschovias 1985). However, these analytic estimates did not account for the change in the magnetic field configuration during the protostellar phase. Most of the protostellar phase was also

missed in the pioneering 3D ideal MHD simulations of magnetic braking of Matsumoto & Tomisaka (2004) and in non-ideal MHD simulations of Masson et al. (2016), who did not find a significant effect of magnetic alignment on braking efficiency.

Testing these magnetic braking scenarios is complicated by the fact that other mechanisms unrelated to the magnetic field, such as self-scattering of the dust’s thermal emission, can generate polarized continuum emission. Self-scattering is inefficient on large cloud scales because the grains are too small ($a \sim \mu\text{m}$) to scatter millimeter-wavelength light efficiently. On the disk-scale, where the grains could be much larger, new theoretical studies (e.g., Kataoka et al. 2015, 2016a; Yang et al. 2016a, 2016b) have shown that scattering may in fact produce the polarization observed in some protostellar disks (Rao et al. 2014; Stephens et al. 2014; Cox et al. 2015; Segura-Cox et al. 2015; Fernández-López et al. 2016; Kataoka et al. 2016b). This mechanism may be useful because it can be used to probe the size of the dust grains observed, independent of the spectral index (α), using the scattering cross-section as a proxy (Kataoka et al. 2015, 2016a). This may be a good alternative to measuring the grain size using the spectral index because α is degenerate in areas of high optical depth or low temperatures, such as young disks. Since grains are expected to grow more easily in a dense, rotationally supported disk than in a rapidly infalling envelope, grains are more likely to exhibit scattering-induced polarization in disks than in envelopes. Polarization in disks and envelopes may therefore have different origins.

Another mechanism for producing polarized emission is direct alignment of the grains via radiation pressure. Lazarian & Hoang (2007) first discussed this mechanism, and Tazaki et al. (2017) have shown that, in a disk, instead of aligning with an external magnetic field, large grains may align with their short axes along the direction of the radiative flux anisotropy. This would produce an azimuthal polarization pattern in a disk. The aligning photons may be in the far-infrared and may not come directly from the star. Kataoka et al. (2017) and Stephens et al. (2017b) have demonstrated that scattering and radiative alignment dominate the emission at 850 μm and 3 mm, respectively, in the Class I/II source HL Tau.

While each of the three scenarios predicts different detailed structures in the polarization emission in disks/envelopes, previous observations have not been able to disentangle them due to comparatively poor resolution ($\gtrsim 2''5$, ~ 400 au to 1000 au depending on the cloud), leading to disk/envelope confusion. High-resolution observations are needed to accurately probe each structure. In this paper, we present Atacama Large Millimeter/submillimeter Array (ALMA) 870 μm dust continuum polarization observations of 10 Class 0/I protostars in the Perseus Molecular Cloud.

2. Observation and Sample Selection

2.1. Sample Selection

Our target selection was constructed from our Very Large Array Nascent Disk and Multiplicity (VANDAM) survey (Tobin et al. 2015, 2016). The VANDAM sources include all 94 identified protostellar systems in the Perseus Molecular Cloud ($d \sim 230$ pc; Hirota et al. 2008); as part of the survey, they were imaged at both Ka (8 mm/1 cm) and C (4/6 cm)

bands. Of these, we have preliminarily defined some of the sources as being “disk-candidates,” which means that they are resolved (perpendicular to the outflow direction when known) and that their emission profiles were fit by a model of a self-similar, viscously evolving density profile with a reasonable temperature profile (see Segura-Cox et al. 2016); this excluded some extended sources (see Segura-Cox 2017). For this paper, we started with the full VANDAM sample, then chose the brightest 25 at 220 GHz from the Submillimeter Array (SMA) Mass Assembly of Stellar Systems and their Evolution (MASSES) survey (K. Lee 2018, private communication). Of those, we selected the expected brightest in ALMA Band 7 assuming reasonable values for the 8 mm–870 μm spectral index. Finally, we only observed the 10 sources with no previous polarimetric observations in the millimeter/centimeter bands. Of these 10 sources, only 3 protostars (Per-emb-11, Per-emb-14, and Per-emb-50) were identified as Class 0/I disk-candidates in Segura-Cox (2017). The other 7 sources (hereafter, “non-disk-candidates”), whose 8 mm emission could not be fit in Segura-Cox (2017), included two (Per-emb 2 and 18) whose morphologies resemble a fragmenting disk, but could not be fit by the model, and one close binary (Per-emb 5).

2.2. Observations and Data Reduction

The data were taken using ALMA Band 7 on 2016 July 17 in configuration C40-4 (project code 2015.1.01503.S; PI: Erin Cox). Our observations were taken in full polarization mode, with four spectral windows tuned for continuum observations. The observations took a total of 2.6 hr, with ~ 8 minutes spent per source. Baselines for the C40-4 configuration ranged from 15 to 704 m, corresponding to a maximum recoverable scale of $\sim 7''.2$ and a resolution of $\sim 0''.35$. The four spectral windows were centered on 337.5, 339.4, 347.5, and 349.5 GHz. The sources J0336+3218, J0238+1636, J0237+2848, and J0510+1800 were used to calibrate the phase, flux, bandpass, and polarization, respectively. J0319+3101 was used as the check calibrator for the phase transfer. The overall amplitude calibration uncertainty at Band 7 for ALMA is 10%; we only report the statistical uncertainties on the flux densities reported in this paper. The absolute calibration uncertainty in the polarization position angle is $\sim 0^\circ.4$ (Nagai et al. 2016), which is smaller than the statistical uncertainties for these sources.

These observations were reduced manually by data analysts at the National Radio Astronomy Observatory (NRAO), using the Common Astronomy Software Applications (CASA) package (McMullin et al. 2007), version 4.7.0. These calibrations included first applying a priori calibrations, such as baseline corrections and phase corrections from water vapor radiometer measurements. Then, bandpass calibration, flux calibration, and antenna gain calibrations were carried out. Polarimetric calibration was then done. First, the polarization properties of J0510+1800 were roughly estimated by solving for gain ratio of the linearly polarized feeds, X and Y. Then, the cross-hand delays and residual $X - Y$ phase were solved for, and the Stokes Q/U ambiguity in the calibration was resolved through examination of the X/Y gain ratios. With this, the source properties were determined. The final step was to calibrate the polarization leakage, or D -terms. The parallactic angle coverage for J0510+1800 was sufficient to allow the calibration of both source properties and D -terms.

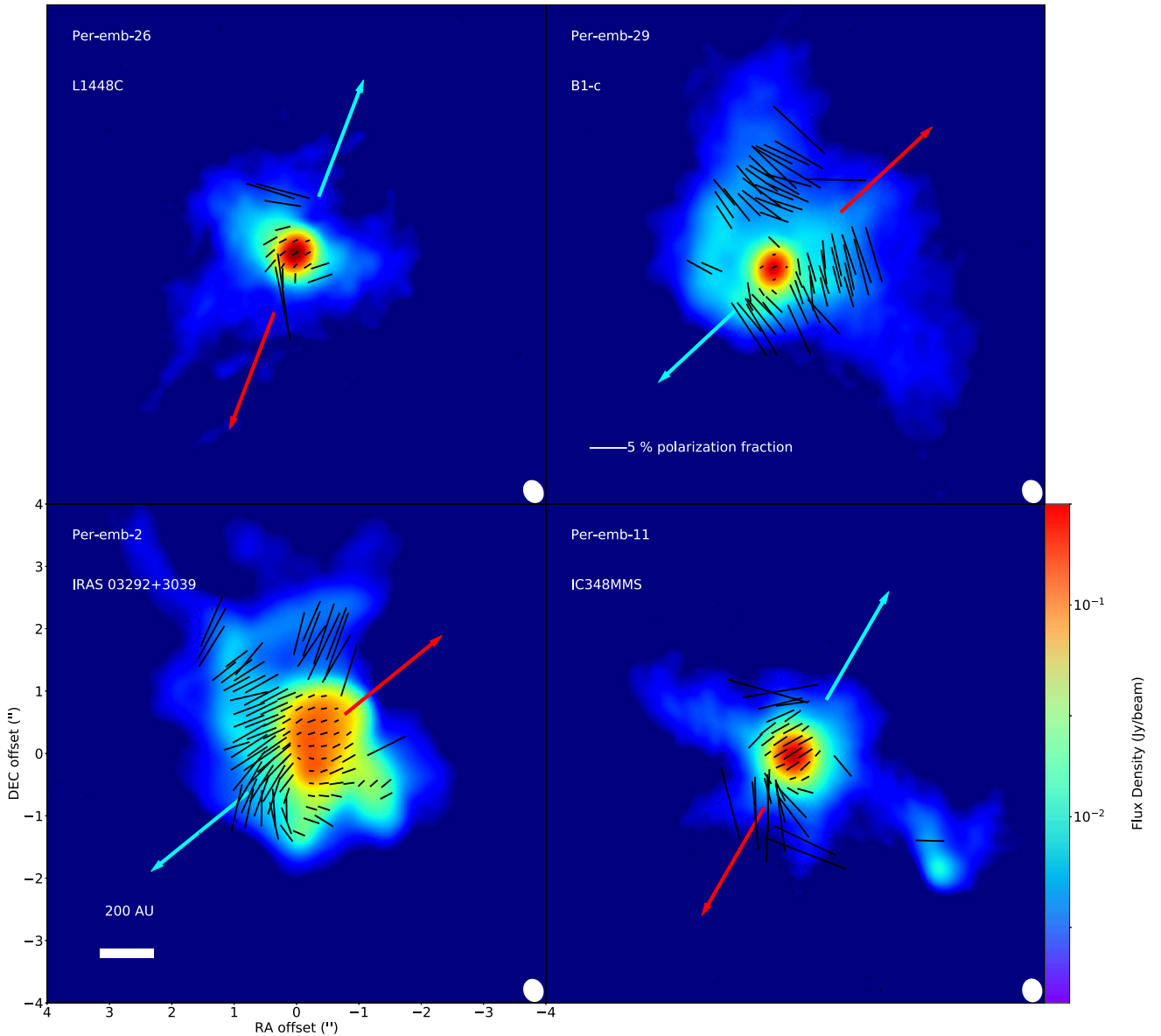


Figure 1. 870 μm dust continuum emission is shown in colorscale. Black vectors show the (non-rotated) polarization. Their length corresponds to the polarization fraction. Outflow directions are shown with red and blue arrows, and the beam is in the bottom right corner. These four sources have significant large-scale emission from their envelopes. These maps were made using emission above 5σ (~ 47 mJy) in polarized intensity.

For all but one of the targets, Per-emb-41, we performed one iteration of a phase-only self-calibration over the integration time to improve the signal-to-noise ratio (S/N) in the images. Per-emb-41, however, was bright enough to self-calibrate over a 6 s interval. We used the CASA task CLEAN, with natural weighting, to produce the final, full Stokes images for all sources. The typical resolution for our observations was $0''.38$ by $0''.31$.

Our calibrated images were used to make polarization intensity, polarization angle, and polarization fraction maps. To do this, we used the CASA task immath. The linear polarization intensity map represents the quantity $\sqrt{Q^2 + U^2}$, and the polarization angle map represents the quantity $0.5 \arctan(U/Q)$. The polarization intensity maps were debiased using the average noise value determined from the Q and U maps. Each map was masked below 5σ . The linear polarization fraction map was then formed by dividing the linear polarization map by the Stokes I map.

3. Results

In Figures 1 and 2, we show images of our sources. In Table 1, we summarize the results. Integrated and peak flux densities are estimated from elliptical Gaussian fits using the CASA task imfit. We also present the polarization properties and outflow angles (taken from Stephens et al. 2017a and references therein). We detect polarization at a $\gtrsim 5\sigma$ level in each source. Because the polarization is relatively well ordered inside of ~ 150 au of each protostar, we present the average polarization angle within this region. The average polarization angle is estimated by forming the polarized-intensity weighted average, i.e.,

$$\langle \theta \rangle = \frac{\sum_i P_i \theta_i}{\sum_i P_i}, \quad (1)$$

where P_i is value of the linearly polarized intensity in pixel i and θ_i is the polarization position angle in the same pixel. The

Table 1
Perseus Polarization

| Object | Alternate Name | R.A. | Decl. | I Peak Flux | Integrated Flux | Polarization Percentage | Polarization Angle | Angle Offset from Outflow |
|-------------------------|------------------|--------------|---------------|---------------------------|-----------------|-------------------------|--------------------|---------------------------|
| | | (J2000) | (J2000) | (mJy beam ⁻¹) | (mJy) | % | (°) | (°) |
| Per-emb-26 | L1448C, L1448-mm | 03:25:38.875 | +30:44:05.281 | 284.2 ± 3.3 | 354.2 ± 6.6 | 1.0 ± 0.1 | 123.4 | 35.6 |
| Per-emb-50 ^a | | 03:29:07.769 | +31:21:57.098 | 166.4 ± 0.6 | 192.9 ± 1.2 | 2.3 ± 0.1 | 96.1 | 0.9 |
| Per-emb-21 | | 03:29:10.668 | +31:18:20.156 | 94.3 ± 1.2 | 105.5 ± 2.3 | 1.1 ± 0.1 | 116.2 | 68.2 |
| Per-emb-18 | NGC1333 IRAS7 | 03:29:11.266 | +31:18:31.087 | 127.4 ± 4.2 | 365 ± 16 | 1.1 ± 0.2 | 97.1 | 52.9 |
| Per-emb-14 ^a | NGC1333 IRAS4C | 03:29:13.549 | +31:13:58.107 | 115.8 ± 1.3 | 186 ± 3.1 | 1.6 ± 0.1 | 105.2 | 10.2 |
| Per-emb-5 | IRAS 03282+3035 | 03:31:20.939 | +30:45:30.252 | 291.6 ± 3.1 | 501.8 ± 7.9 | 0.8 ± 0.1 | 0.0 | 55.0 |
| Per-emb-2 | IRAS 03292+3039 | 03:32:17.923 | +30:49:47.824 | 116.8 ± 5.8 | 1216 ± 66 | 1.9 ± 0.3 | 106.5 | 22.5 |
| Per-emb-29 | B1-c | 03:33:17.878 | +31:09:31.775 | 193.7 ± 5.4 | 268 ± 12 | 5.5 ± 1.2 | 112.9 | 50.4 |
| Per-emb-41 | B1-b | 03:33:20.341 | +31:07:21.322 | 19.42 ± 0.14 | 19.42 ± 0.14 | 1.5 ^b | 125.2 | 87.8 |
| Per-emb-11 ^a | IC348MMS | 03:43:57.067 | +32:03:04.762 | 209.2 ± 4.5 | 397 ± 12 | 2.0 ± 0.2 | 122.5 | 27.4 |

Notes.

^a Indicates a source identified as a disk-candidate on the basis of fitting the 8 mm visibility profile (Segura-Cox et al. 2016).

^b Indicates that `imfit` failed to converge to a solution for the polarized intensity of Per-emb-41 and this value was computed using the peak polarized intensity and the peak Stokes I.

Polarization percentage was found by first running `imfit` on Stokes I and the polarization intensity maps and then dividing them. The uncertainties are quoted in percentage and were found using the respective uncertainties of the fits for the source-integrated values of Stokes I and polarized intensity. Since the polarized-intensity map of Per-emb-41 was unable to be fit, it has no quoted uncertainty. Polarization angle values were found using a radius of 0.5'' in each source. Uncertainties in the polarization angle over this range are $\lesssim 1^\circ$. The values quoted represent the non-rotated, polarization values, consistent with Figures 1 and 2.

sum is taken within a circle of radius 115 au ($=0.5$ arcsec) centered at the peak of the polarized continuum.

In all sources, regardless of their classification as disk-candidate/non-disk-candidate sources (via their 8 mm emission), we find a significant difference in the small-scale polarization structure near the central protostar and the larger-scale polarization structure in the envelope. The morphology and percentage of the inner (disk) and of the outer (envelope) regions starkly contrast. To quantify the effects of the differing polarization fraction limits in the inner regions versus the outer envelopes in our maps, we computed the lowest detectable polarization fraction in the outer regions. We find that the higher polarization fractions in the outer envelope are not merely marginally detected due to the lower sensitivity to polarization fraction in the envelope. On the contrary, the typical detection is at a level ~ 2 times the minimum detection threshold.

To further quantify this, we used the `lifelines` Python package (Davidson-Pilon et al. 2017)⁷ to compute the Kaplan–Meier product limit estimator for the probability distribution for polarization percentage. This quantity is essentially a cumulative probability distribution function (CDF) that can incorporate upper limits. To construct these, we sample the polarization fraction (or its upper limit) at spacings of $\sim 1/2$ beam-width (to ensure a degree of statistical independence). These samples are put into two categories: those samples within ~ 100 – 150 au in projected separation from the protostar and those outside this range. The data from all 10 protostars are combined. These distributions are shown in Figure 4. They clearly show that the inner/outer regions have similar distributions of polarization fraction up to $\sim 1\%$ – 2% , but that the outer regions have a significantly higher chance of exhibiting a large value (\gtrsim few %) as compared to the inner regions. The p -value for the log-rank test between the two classes is $p \lesssim 10^{-4}$.

The angular offset ($\Delta\theta$) distribution of the polarization from the outflow axis is an observable that relates to the efficacy of magnetic braking during the accretion process. We performed

both the Kolmogorov–Smirnov (KS) and Anderson–Darling (AD) tests to compare the distribution of $\Delta\theta$ to that of a uniform distribution. These results are summarized in Figure 5. We find suggestive evidence ($p \sim 0.02$ – 0.06) that the angular offset differs from a uniform random variable between 0° and 90° for the three disk-candidate sources in our sample and that the distribution of angular offsets for the disk-candidate sources is different than for the non-disk-candidate sources. We find no evidence ($p \gtrsim 0.3$) that the offset distribution for the non-disk-candidate sources is different from a random uniform distribution.

While the polarization structure of the inner regions (on the disk-scale) of the protostellar environment is relatively uniform, that of the envelope is not. In all sources for which significant envelope is detected, we find complex structure in the polarization morphology. Figure 3 shows the four sources in our sample (Per-emb-2, Per-emb-5, Per-emb-11, and Per-emb-29) with relatively complicated envelope polarization. The polarization vectors have been rotated by 90° under the assumption that the mechanism responsible for the polarized emission is magnetically aligned dust grains. Per-emb-5, Per-emb-11, and Per-emb-29 show some morphological similarities to the hourglass morphology expected if the polarization traces magnetic field lines dragged in by accreting material (as observed by, e.g., Girart et al. 2006; Rao et al. 2009; Stephens et al. 2013). In the case of Per-emb-2, the morphology in the center, toward the south, and toward the northeast resembles this, but the polarization due east and due north is orthogonal to the expected direction.

The morphology of the total dust emission from all the sources is also interesting. Very detailed and intricate $870 \mu\text{m}$ dust emission surrounds the young sources. We see a clear distinction between the younger, Class 0 sources and the older, Class I sources (Per-emb-41 and Per-emb-50). Younger sources show a dust envelope that clearly has structure (see Figures 1 and 2), much of which is filamentary or at least not-spherical in nature (e.g., Looney et al. 2007; Tobin et al. 2010; Lee et al.

⁷ This package is available at <https://github.com/CamDavidsonPilon/lifelines/>.

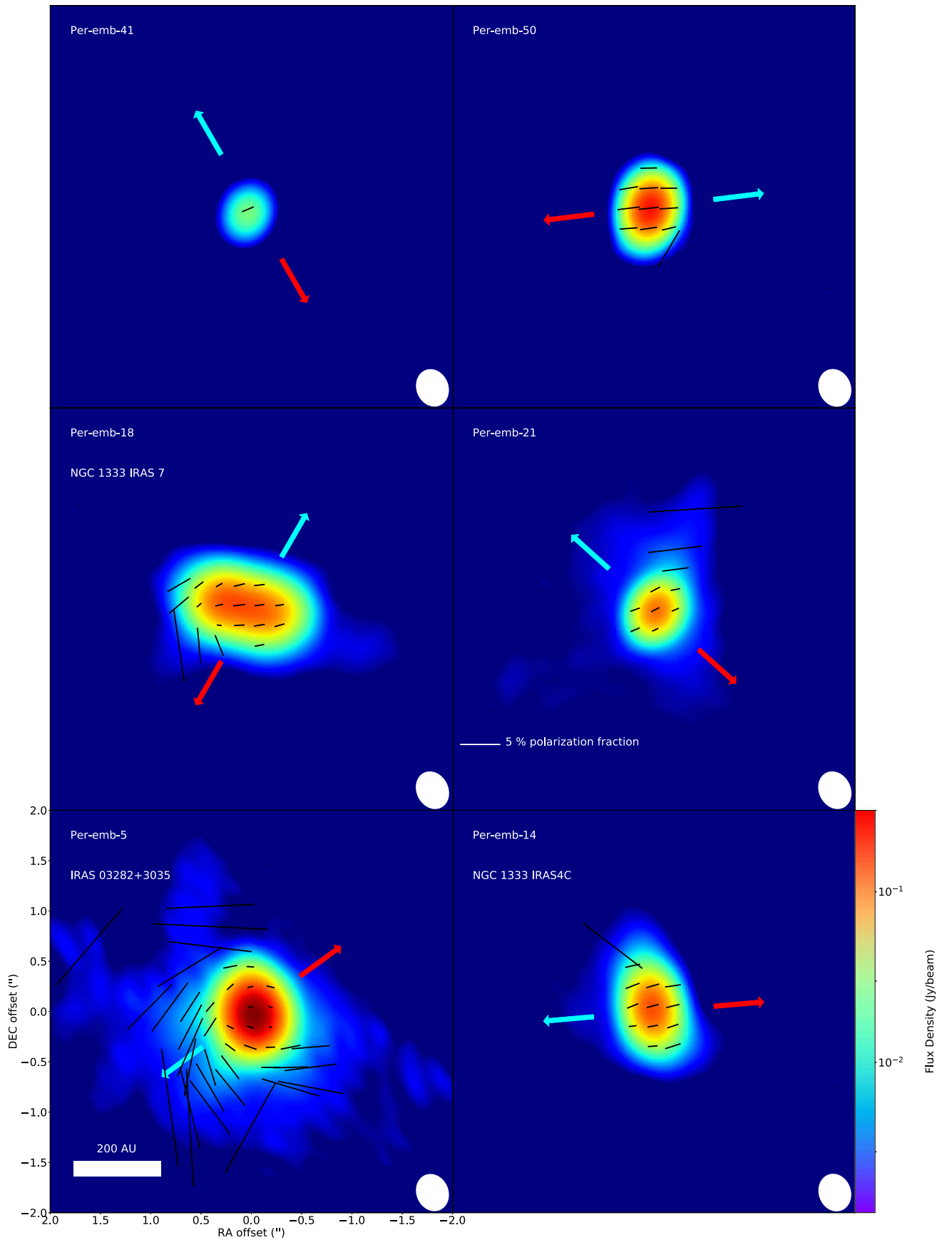


Figure 2. 870 μm dust continuum emission is shown in colorscale. Black vectors show the (non-rotated) polarization. Their length corresponds to the polarization fraction. Outflow directions are shown in red and blue arrows, and the beam is in the bottom right corner. These six are more compact and are zoomed in compared to Figure 1. These maps were made using emission above 5σ (~ 47 mJy) in polarized intensity.

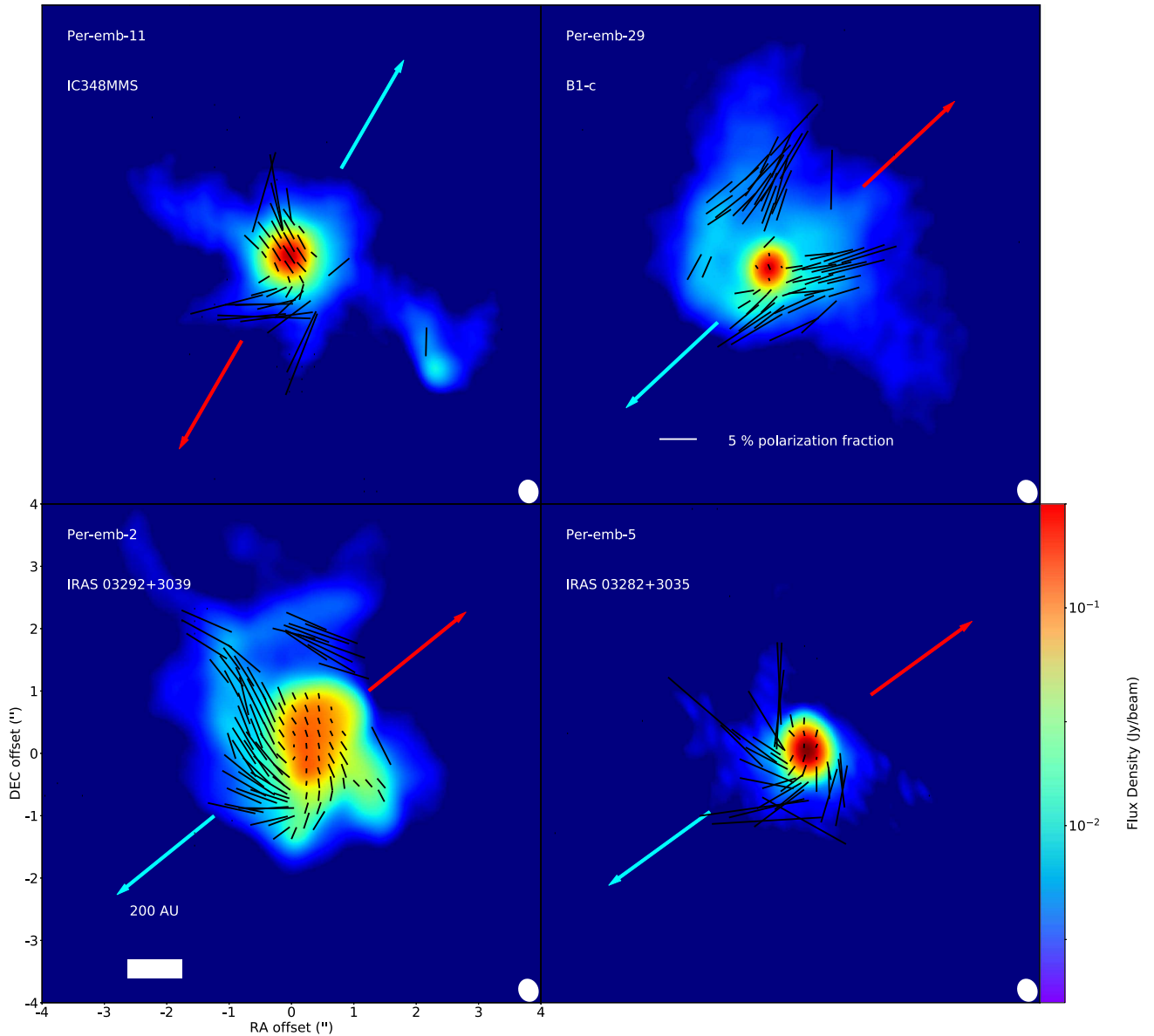


Figure 3. 870 μm observations of our sources with significant envelope emission shown in colorscale. In this figure, black vectors are rotated (90°) polarization vectors, showing the plane-of-sky inferred magnetic field. Their length corresponds to the polarization fraction. Outflow directions are shown with red and blue arrows. The beam is in the bottom right corner.

2012). The older sources, on the other hand, do not show much envelope emission surrounding the protostar.

4. Discussion

Our principle survey goal was to examine the polarization structure of a set of young protostars to see whether we could explain it in the context of models that predict polarization due to different mechanisms, i.e., direct emission from magnetically aligned dust (Lazarian 2007), thermal self-scattering (Kataoka et al. 2016a), and direct emission from dust aligned by radiative flux (Tazaki et al. 2017). Our data provide a unique view into this important topic.

The inner ~ 150 au of each source shows a relatively well ordered polarization structure. In some sources (Per-emb-2, 5, 26), there is morphological evidence for a smooth gradient in the position angle across the source. In others, the polarization position angle is constant to within a few degrees. Of particular

interest are the sources with candidate 8 mm disks (Per-emb-11, 14, 50), where the constant polarization position angle is aligned (for Per-emb 14 and 50 to within about 10° , and for Per-emb-11 to within 20°) with both the minor axis of the disk and with the outflow axis. Figure 5 provides quantitative evidence for this. Such a signature is broadly consistent with an origin in self-scattering in the disks, wherein the polarization is parallel to the disk’s minor axis. This morphology may also be consistent with magnetically aligned grains as well. While the polarization angle shows virtually no change in the inner region, these disks’ inclinations range from $\sim 45^\circ$ – 65° (Segura-Cox et al. 2016), making it unclear whether the change in polarization angle due to grains aligned with respect to a toroidal magnetic field would be obvious. However, the uncertainty in the inclination angle is $\sim 10^\circ$, which means that it is plausible that these sources are nearly edge-on, in which case no change in the polarization position angle across the source would be observed. It is unclear the degree to which the

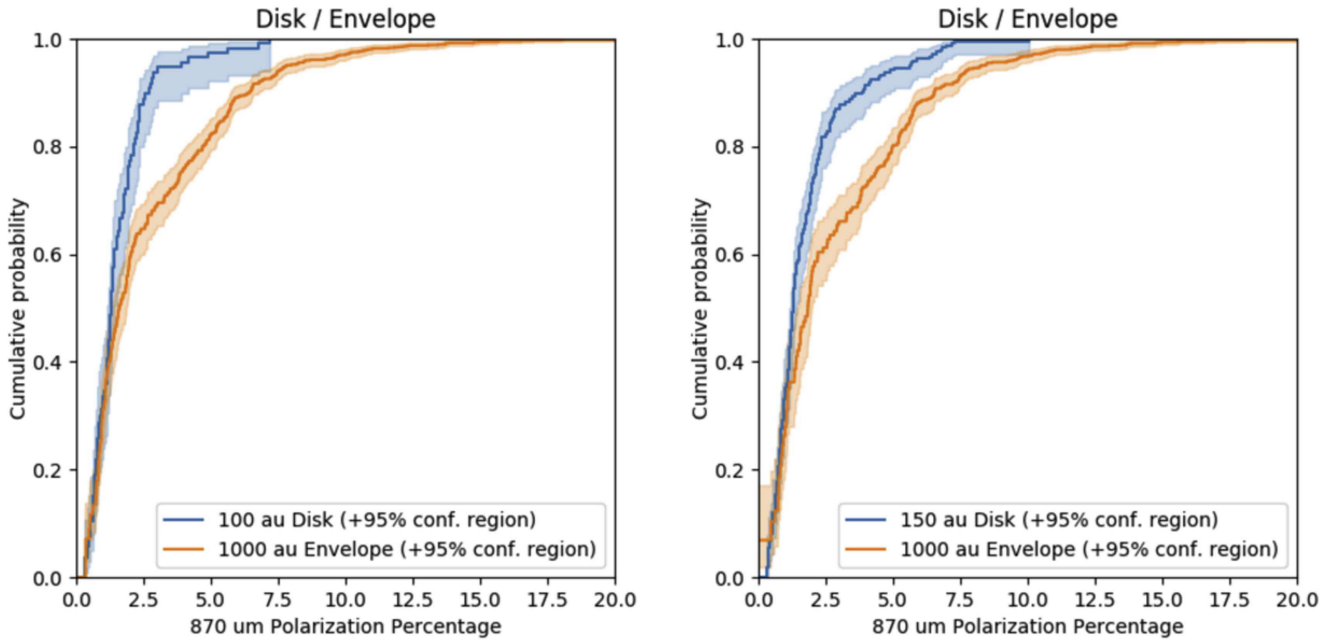


Figure 4. Disk and envelope KM product limit estimators for two “disk” sizes, 100 au and 150 au, with an “envelope” size of 1000 au. These were made by combining the polarization information for all 10 sources. The shaded area represents the 95% confidence region for the KM estimator. Note the drastic difference between the disk and the envelope no matter which radius is used.

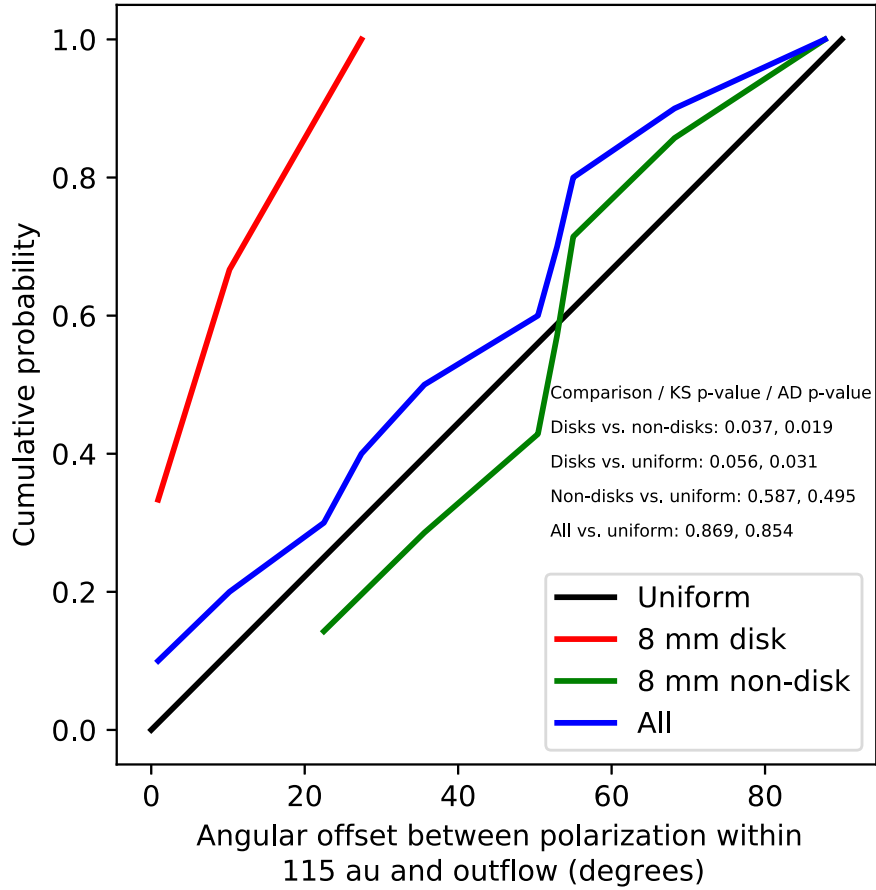


Figure 5. Distribution of the angular offset of the small-scale polarization angle and the outflow angle as projected onto the sky. Sources are both divided into disk-candidates at 8 mm (red) and those that are not (green), as well as all combined (blue). The distribution for a uniform distribution is shown in black. P -values for the comparison of the disk-candidates/non-disk-candidate/uniform distributions for both the KS (left) and AD (right) statistical tests are given. Note that while the disk-candidate line is quite far from the uniform line, the p -values are high. This is likely due to our small (3) sample size.

inner envelope in these sources (as opposed to the disk) is contributing to the polarization signal. In the non-disk-candidate sources, the polarization is essentially randomly oriented with respect to the outflow axis, which is very different from the disk-candidate sources.

Our data show a stark contrast in the polarization levels near the protostar and in the envelope. This “polarization hole” has been observed in both prestellar cores and protostars (Dotson 1996; Matthews et al. 2002; Girart et al. 2006; Liu et al. 2013; Hull et al. 2014). This suggests that the polarization in the envelope inherently differs from the polarization in the region near the protostar. Though we cannot definitively state the cause of this hole, there are a few possibilities. One is that the grains are magnetically aligned and that the magnetic field becomes more tangled in the inner regions. Such a scenario has been suggested for such polarization holes observed in single-dish (Dotson 1996) and interferometric (Hull et al. 2014) surveys. For our sources, this would imply that the field near the protostar is disordered even at $\lesssim 20$ au size-scales. Another possibility is the difference in grain sizes between the outer envelope and inner envelope/disk. It is likely that the grains near the protostar have grown much larger than those in the envelope. It is also plausible that small grains are more non-spherical and aligned easily by magnetic fields, so it could be that this alignment dominates the envelope polarization. Third, regardless of the mechanism that produces the polarization, optical depth effects may play a role. For both scattering and emission from magnetically aligned grains, the polarization at low/intermediate τ is higher than that at $\tau \gtrsim 1$ (Yang et al. 2017), although polarized thermal emission is expected to decline more rapidly than polarization from scattering as optical depth increases. Finally, the inner-region polarization could be from a different mechanism, such as scattering or radiatively aligned grains, that could conceivably result in a lower polarization percentage. Self-scattering is expected to yield $\sim 1\%$ of polarization fraction (e.g., Stephens et al. 2014; Yang et al. 2016a), which is close to what we see in the inner regions. Alternatively, radiative alignment will have similar fractional polarization to magnetically aligned grains, except close to the central regions, where the polarization may decrease as the optical depth increases (see Equation (5) in Andersson et al. 2015). An interesting possibility is that the areas of low ($\sim 1\%$) polarization might not be a true rotationally supported disk, but instead an infalling envelope. In this scenario, perhaps both the inner and outer regions harbor magnetically aligned grains, just aligned to different extents. If this is the case, the rapid change of polarization direction between the inner and outer envelopes observed in our non-disk-candidate sample points to a quite complex magnetic field morphology in the transition region on 10^2 – 10^3 au scales.

5. Summary





We have presented our $870\ \mu\text{m}$ dust polarization survey of 10 protostars using ALMA. These sources consist of three disk-candidates and seven non-disk-candidate sources. All sources show significant levels of polarized emission, and most show a stark contrast in both their morphology and polarization percentage between the inner and outer regions. We find evidence that our disk-candidates show a polarization signature akin to either self-scattering in their inner region or grains aligned with a toroidal field in an inclined disk, while the non-disk-candidate sources show a randomly aligned polarization

angle. We also have shown that the morphologies and percentage levels in the extended envelope emission are very different, and that it may be dominated by another mechanism, most likely by magnetically aligned grains. Additional modeling and multi-wavelength observations are needed to further disentangle the different polarization mechanisms in these young sources.

We thank the anonymous referee for their helpful comments. We thank Katherine Lee and the VANDAM team for invaluable work on the source list. E.G.C. is supported by SOSP3-017. H.F.Y. is supported in part by an SOS award from NRAO and Z.Y.L. by NASA NNX 14AB38G, NSF AST-1313083, and 1716259. This paper makes use of the following ALMA data: ADS/JAO.ALMA#2015.1.01503.S. ALMA is a partnership of ESO (representing its member states), NSF (USA) and NINS (Japan), together with NRC (Canada), NSC and ASIAA (Taiwan), and KASI (Republic of Korea), in cooperation with the Republic of Chile. The Joint ALMA Observatory is operated by ESO, AUI/NRAO and NAOJ. The NRAO is a facility of the National Science Foundation operated under cooperative agreement by Associated Universities, Inc.

Software: CASA (v4.7.0; McMullin et al. 2007), lifelines (Davidson-Pilon et al. 2017), Matplotlib (<https://doi.org/10.1109/MCSE.2007.55>).

ORCID iDs

Erin G. Cox  <https://orcid.org/0000-0002-5216-8062>
 Leslie W. Looney  <https://orcid.org/0000-0002-4540-6587>
 John J. Tobin  <https://orcid.org/0000-0002-6195-0152>
 Ian Stephens  <https://orcid.org/0000-0003-3017-4418>

References

- Andersson, B.-G., Lazarian, A., & Vaillancourt, J. E. 2015, *ARA&A*, **53**, 501
- Andre, P., Ward-Thompson, D., & Barsony, M. 1993, *ApJ*, **406**, 122
- Andrews, S. M., Wilner, D. J., Hughes, A. M., Qi, C., & Dullemond, C. P. 2009, *ApJ*, **700**, 1502
- Andrews, S. M., Wilner, D. J., Hughes, A. M., Qi, C., & Dullemond, C. P. 2010, *ApJ*, **723**, 1241
- Balbus, S. A., & Hawley, J. F. 1998, *RvMP*, **70**, 1
- Beckwith, S. V. W., Sargent, A. I., Chini, R. S., & Guesten, R. 1990, *AJ*, **99**, 924
- Blandford, R. D., & Payne, D. G. 1982, *MNRAS*, **199**, 883
- Chapman, N. L., Davidson, J. A., Goldsmith, P. F., et al. 2013, *ApJ*, **770**, 151
- Cox, E. G., Harris, R. J., Looney, L. W., et al. 2015, *ApJL*, **814**, L28
- Dapp, W. B., & Basu, S. 2010, *A&A*, **521**, L56
- Davidson-Pilon, C., Kalderstam, J., Kuhn, B., et al. 2017, lifelines.py, v0.11.1, Zenodo, doi:10.5281/zenodo.815943
- Dotson, J. L. 1996, *ApJ*, **470**, 566
- Fernández-López, M., Stephens, I. W., Girart, J. M., et al. 2016, *ApJ*, **832**, 200
- Girart, J. M., Rao, R., & Marrone, D. P. 2006, *Sci*, **313**, 812
- Hennebelle, P., & Fromang, S. 2008, *A&A*, **477**, 9
- Hirota, T., Bushimata, T., Choi, Y. K., et al. 2008, *PASJ*, **60**, 37
- Hull, C. L. H., Girart, J. M., Tychoniec, L., et al. 2017, *ApJ*, **847**, 92
- Hull, C. L. H., Plambeck, R. L., Kwon, W., et al. 2014, *ApJS*, **213**, 13
- Hunter, J. D. 2007, *CSE*, **9**, 90
- Joos, M., Hennebelle, P., & Ciardi, A. 2012, *A&A*, **543**, A128
- Kataoka, A., Muto, T., Momose, M., et al. 2015, *ApJ*, **809**, 78
- Kataoka, A., Muto, T., Momose, M., Tsukagoshi, T., & Dullemond, C. P. 2016a, *ApJ*, **820**, 54
- Kataoka, A., Tsukagoshi, T., Momose, M., et al. 2016b, *ApJL*, **831**, L12
- Kataoka, A., Tsukagoshi, T., Pohl, A., et al. 2017, *ApJL*, **844**, L5
- Lazarian, A. 2007, *JQSRT*, **106**, 225
- Lazarian, A., & Hoang, T. 2007, *MNRAS*, **378**, 910
- Lee, K., Looney, L., Johnstone, D., & Tobin, J. 2012, *ApJ*, **761**, 171

- Li, Z.-Y., Banerjee, R., Pudritz, R. E., et al. 2014, in *Protostars and Planets VI*, ed. H. Beuther et al. (Tucson, AZ: Univ. Arizona Press), 173
- Li, Z.-Y., Krasnopolsky, R., & Shang, H. 2011, *ApJ*, 738, 180
- Liu, H. B., Qiu, K., Zhang, Q., Girart, J. M., & Ho, P. T. P. 2013, *ApJ*, 771, 71
- Looney, L. W., Tobin, J. J., & Kwon, W. 2007, *ApJL*, 670, L131
- Masson, J., Chabrier, G., Hennebelle, P., Vaytet, N., & Commerçon, B. 2016, *A&A*, 587, A32
- Matsumoto, T., & Tomisaka, K. 2004, *ApJ*, 616, 266
- Matthews, B. C., Fiege, J. D., & Moriarty-Schieven, G. 2002, *ApJ*, 569, 304
- McMullin, J. P., Waters, B., Schiebel, D., Young, W., & Golap, K. 2007, in *ASP Conf. Ser. Astronomical Data Analysis Software and Systems XVI*, 376, ed. R. A. Shaw, F. Hill, & D. J. Bell (San Francisco, CA: ASP), 127
- Mellon, R. R., & Li, Z.-Y. 2008, *ApJ*, 681, 1356
- Mellon, R. R., & Li, Z.-Y. 2009, *ApJ*, 698, 922
- Mouschovias, T. C. 1985, *A&A*, 142, 41
- Nagai, H., Nakanishi, K., Paladino, R., et al. 2016, *ApJ*, 824, 132
- Rao, R., Girart, J. M., Lai, S.-P., & Marrone, D. P. 2014, *ApJL*, 780, L6
- Rao, R., Girart, J. M., Marrone, D. P., Lai, S.-P., & Schnee, S. 2009, *ApJ*, 707, 921
- Segura-Cox, D. M. 2017, PhD thesis Univ. Illinois
- Segura-Cox, D. M., Harris, R. J., Tobin, J. J., et al. 2016, *ApJL*, 817, L14
- Segura-Cox, D. M., Looney, L. W., Stephens, I. W., et al. 2015, *ApJL*, 798, L2
- Shu, F. H., Adams, F. C., & Lizano, S. 1987, *ARA&A*, 25, 23
- Stephens, I. W., Dunham, M. M., Myers, P. C., et al. 2017a, *ApJ*, 846, 16
- Stephens, I. W., Looney, L. W., Kwon, W., et al. 2013, *ApJL*, 769, L15
- Stephens, I. W., Looney, L. W., Kwon, W., et al. 2014, *Natur*, 514, 597
- Stephens, I. W., Yang, H., Li, Z.-Y., et al. 2017b, *ApJ*, 851, 55
- Tazaki, R., Lazarian, A., & Nomura, H. 2017, *ApJ*, 839, 56
- Tobin, J. J., Dunham, M. M., Looney, L. W., et al. 2015, *ApJ*, 798, 61
- Tobin, J. J., Hartmann, L., Looney, L. W., & Chiang, H.-F. 2010, *ApJ*, 712, 1010
- Tobin, J. J., Looney, L. W., Li, Z.-Y., et al. 2016, *ApJ*, 818, 73
- Yang, H., Li, Z.-Y., Looney, L., & Stephens, I. 2016a, *MNRAS*, 456, 2794
- Yang, H., Li, Z.-Y., Looney, L. W., et al. 2016b, *MNRAS*, 460, 4109
- Yang, H., Li, Z.-Y., Looney, L. W., Girart, J. M., & Stephens, I. W. 2017, *MNRAS*, 472, 373
- Zhang, Q., Qiu, K., Girart, J. M., et al. 2014, *ApJ*, 792, 116